

Collective optical behavior from coupled quantum dots visualized by wavelength-resolved and polarization-resolved super-resolution microscopy

Duncan Ryan (✉ ryand@lanl.gov)

Los Alamos National Laboratory <https://orcid.org/0000-0001-7702-8499>

Megan Dunlap

Colorado State University

Jennifer Hollingsworth

Los Alamos National Laboratory

Somak Majumder

Los Alamos National Laboratory

Martin Gelfand

Colorado State University

James Werner

Los Alamos National Laboratory

Alan Van Orden

Colorado State University

Peter Goodwin

Los Alamos National Laboratory

Article

Keywords:

Posted Date: May 12th, 2022

DOI: <https://doi.org/10.21203/rs.3.rs-1297011/v1>

License:   This work is licensed under a Creative Commons Attribution 4.0 International License.

[Read Full License](#)

Collective optical behavior from coupled quantum dots visualized by wavelength-resolved and polarization-resolved super-resolution microscopy

Duncan P. Ryan^{1,}, Megan K. Dunlap², Jennifer A. Hollingsworth¹, Somak Majumder¹, Martin P. Gelfand³, James H. Werner¹, Alan van Orden², and Peter M. Goodwin¹*

¹Center for Integrated Nanotechnologies, Los Alamos National Laboratory, Los Alamos, New Mexico, 87545, USA

²Department of Chemistry, Colorado State University, Fort Collins, Colorado, 80523, USA

³Department of Physics, Colorado State University, Fort Collins, Colorado, 80523, USA

*E-mail: ryand@lanl.gov

Abstract

Applications of colloidal semiconductor quantum dots (QDs) that place particles into close proximity with other QDs must contend with the effects of interactions between the particles. Electronic coupling facilitates energy transfer, but these environments can also alter the native properties of the individual QDs. How QDs behave collectively due to coupling is a largely unexplored topic. We developed a super-resolution wavelength-resolving and polarization-resolving microscope to capture correlations among the signatures QD coupling. Nanoassemblies containing 2–10 QDs exhibited features of energy transfer: regions of high fluorescence activity from exciton funneling to acceptor particles, and spectral-intensity distributions consistent with donor/acceptor relationships. Spatial distributions of these features were localized with ~ 10 nm precision, on the order of the size of individual particles. Unexpectedly, polarization signatures from nanoassemblies were uniform, indicating a single emission polarization state for a group of QDs. This demonstrates a strong electronic coupling that alters the native behavior of the individual particles.

Many applications of colloidal semiconductor quantum dots (QDs) do not involve isolated particles. QD solids, films, aggregates, and oligomers bring individual particles into close physical proximity where they interact via electromagnetic coupling[1], charge-carrier delocalization[2, 3], and energy transfer[4, 5]. Because of particle coupling, the optical behavior of a nanoassembly is not simply the sum of its components. The range of coupling strengths dictates the degree to which a nanoassembly presents as a collection of individual, isolated particles, or resembles a monolithic emitter. Separation distance, spectral overlap, and dipole-moment alignment are important properties that determine particle coupling efficiency. The local electromagnetic environment induced by neighboring QDs can also affect emission properties.

The CdSe/CdS system possess a hexagonal crystal structure and emits from a 2D degenerate emission plane that is oriented perpendicular to the c -axis of the nanocrystals (Fig. 1a).

38 The 2D emission plane represents the unique polarization signature for a QD. This link be-
39 tween polarization and crystalline structure has been exploited, for example, to track the
40 spatial and rotational movements of individual QDs[6]. In such wurtzite nanocrystals that
41 are approximately spherical, the c -axis also coincides with a permanent electric-dipole mo-
42 ment[7, 8].

43 Although QDs have native fluorescence properties determined by their structure—emission
44 wavelength, lifetime, and polarization—neighboring particles can alter the local environment
45 and effect change. The fluorescence behavior of individual QDs is susceptible to manipula-
46 tion by external electric[9, 10] and magnetic[11] fields. Neighboring QDs can also generate
47 strong local fields due to their permanent electric-dipole moments. Oriented attachment, for
48 example, is driven by electrostatic dipole interactions[12, 13].

49 Studies of collective behavior in QD nanoassemblies have documented altered fluores-
50 cence properties due to the presence of neighboring particles. Fluorescence intermittency
51 (blinking) can manifest as more rapid intensity modulations that does not resemble the sim-
52 ple superposition of typical single-QD binary blinking observed in non-interacting QDs that
53 are physically separated by tens of nanometers[14, 15]. Förster resonance energy transfer
54 (FRET) describes exciton coupling between QD pairs[4, 16]. Lifetime measurements from
55 QD nanoassemblies have observed multi-component fluorescence decay, indicating FRET
56 donor/acceptor relationships[15, 17]. Excitons funnel to local acceptor particles, produc-
57 ing regions with higher fluorescence activity[18, 19], and inducing spectral shifts to longer
58 wavelengths[20, 21]. As a consequence, excitons are exposed to additional loss pathways,
59 potentially reducing device performance[18]. Photon pair correlation measurements from
60 small interacting QD nanoassemblies have also shown strong single-emitter behavior even
61 in assemblies containing multiple distinct emitters[17, 19, 22]. Thus, the optical behavior
62 from QD nanoassemblies is a complex landscape encompassing both individual and collective
63 features.

64 Because separation distance, spectral properties, and orientation are important factors in
65 the behavior of coupled QD systems, multi-dimensional single-molecule measurements can be
66 particularly informative, if combined. In biological imaging using dyes, simultaneous super-
67 resolution localization and 3D orientation measurements have revealed structural alignments
68 in those systems[23, 24]. A variety of instrumentation methods have been recently devel-
69 oped for such super-resolution orientation microscopy: point-spread function (PSF) analy-
70 sis/engineering[25–33], defocused imaging[34–37], and two-[31, 38] or four-component[39–41]
71 polarization imaging. Other single-molecule microscopy techniques have combined simulta-
72 neous measurements of position and spectral signatures[42, 43], or orientation and spectral
73 signatures[44–46]. However, position, emission spectra, and orientation impact coupling ef-
74 ficiency in QD networks, and a simultaneous measurement of all three has not yet been
75 realized.

76 In this work, we examine the collective behavior of QD nanoassemblies (clusters of 2–10

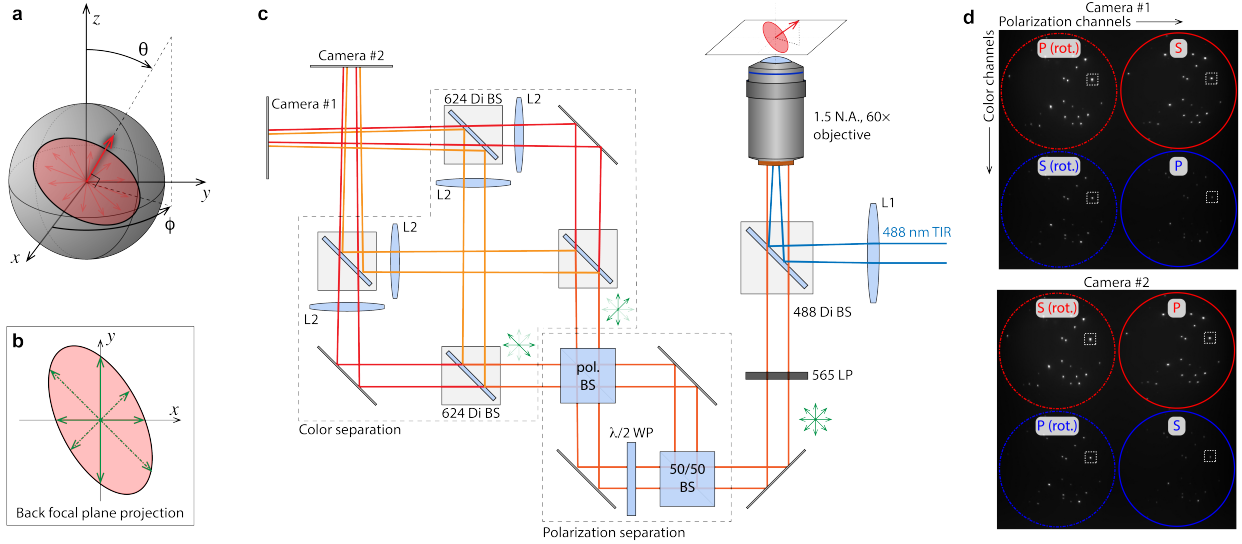
77 particles) by capturing spectral and polarization dynamics, as well as localizing the emis-
78 sion properties with nanometer precision. Previous realizations of polarization microscopy
79 have probed the emission state of single particles[39–41], although these studies were not
80 concerned with nanometer features. We advance super-resolution polarization microscopy
81 by incorporating dual-color optics for wavelength identification, and by providing calibra-
82 tion and analysis methods to correct for biases of imaging in a wide-field configuration.
83 This work is the first demonstration of simultaneous position, wavelength, and polarization
84 measurements of nanoscale emitters, and enables a unique insight into the dynamics of
85 nanoassemblies and their collective behavior.

86 Results

87 Imaging-based polarization microscopy approaches yield higher localization precision com-
88 pared to confocal microscopes that have traditionally been used for polarization measure-
89 ments. While defocused imaging produces the most accurate decomposition of the light-field
90 from an emitter in a single image[36], spreading the signal across more pixels reduces local-
91 ization precision and aberrations in the optical system can distort the PSFs whose unique
92 intensity distributions carry the polarization information. To maximize localization and
93 orientation precision, we implemented a wide-field configuration that images four fixed po-
94 larization components.

95 The wavelength- and polarization-resolving super-resolution microscope setup is illus-
96 trated in Fig. 1. Polarization microscopy probes dipole emission by comparing the inten-
97 sities of different linear projections of the electric field. Orientation information about an
98 emitter can be calculated from the relative strengths of the polarization components. Moni-
99 toring orthogonal polarization components is necessary for normalization. At the back focal
100 plane, the 2D emission plane from a QD is projected into an ellipse, Fig. 1b. Four polariza-
101 tion components are isolated into different optical paths using non-polarizing and polarizing
102 beamsplitters, Fig. 1c, to measure the orientation of the projected polarization ellipse. A
103 half-wave plate rotates the polarizations of one of the polarization pairs 45° . Four matching
104 dichroic beamsplitters provide spectral segmentation, Fig. 1d. S- and P-polarization identi-
105 fiers refer to the polarization components separated by the polarizing beamsplitter. Channels
106 identified as rotated refer to images from the half-wave plate optical paths (-45° and 45°
107 components). Similar polarization microscopy schemes have been reported for single-color
108 measurements, but these works did not address the spatial dependence of correction factors
109 required to analyze the measurements. The color separation dichoric mirrors also introduce
110 additional considerations. Detailed in the Methods section, we present here a solution for the
111 analysis of wide-field polarization measurements that would otherwise bias results, and that
112 is necessary for the more complex optical configuration of dual-color polarization imaging.

113 QDs have unique advantages as emitters for examination with polarization microscopy.



114 Unlike dye molecules, QD excitation above band-edge is isotropic[47]. Therefore, QD nanoassem-
115 blies with potentially differently-oriented QDs do not require complex excitation schemes to
116 ensure homogeneous excitation. Extra considerations due to wobbling dynamics or sub-frame
117 rotational motion typically required for dyes do not apply to QDs fixed to a substrate[29,
118 38].

119 Figure 2 shows time traces of intensity, wavelength, and orientation acquired simultane-
120 ously with the polarization microscope. The intensity trace of a representative single QD
121 (among 29 examined in detail), Fig. 2a, exhibited primarily binary blinking. Under the ex-
122 perimental and environmental conditions, low- and intermediate-intensity gray states[45, 48]
123 were not prominent features. The spectral signature of this QD, Figure 2b, is a single con-
124 stant emission wavelength. For conceptual convenience, polarization anisotropy is converted
125 into the orientation of a 2D emission plane, Fig. 2c. Note that this representation assumes
126 the link between polarization of an ideal 2D emitter and the alignment of its crystalline
127 structure. Here we utilize orientation as a surrogate to describe the emission polarization
128 state. Orientation traces of the polar angle θ and azimuthal angle ϕ for the single QD were
129 also constant.

130 We exploit the intrinsic fluorescence intermittency of QDs to reveal dynamics in QD
131 nanoassemblies. As QDs within a nanoassembly transition between fluorescently bright and
132 dark states, collective emission from the group reflects these configuration changes. In small
133 nanoassemblies the likelihood that all but one emitter go into dark states at some point
134 during a long measurement is high, and it is possible to capture signatures from individual
135 emitters. While a larger nanoassembly may produce a superposition of different optical
136 signatures that blur the polarization state and position, measurements are still sensitive to
137 changes that occur due to fluorescence transitions. As illustrated in Fig. 2a–c, the spectral,
138 spatial, and polarization characteristics of a single QD are constant, but fluorescence intensity
139 is a dynamic property. Figure 2d–f show traces from a small QD nanoassembly. Unlike a
140 single QD, multiple distinct intensity levels were present. The spectral and orientation traces
141 depict sudden changes. Orientation changes occurred exclusively in θ , but were within a
142 narrow range, less than 30° .

143 Figure 3 offers different visualizations of the trace information to emphasize correlations.
144 Localization plots generated from the rotated and non-rotated polarization components,
145 Fig. 3a, show single, well-defined features for an isolated QD. Arrows—whose lengths map
146 θ and directions ϕ for each frame of the measurement—combine the orientation information
147 with the localization map. Figure 3b shows orientation angles mapped onto a polar plot. The
148 two-fold degeneracy of the azimuthal angle is represented by the two features azimuthally
149 separated by 180° . The radial distance indicates how tilted the QD is: markers at the
150 origin if not tilted or markers at the edge of the plot if the c -axis is lying in the focal plane.
151 The spectral-intensity distribution, Fig. 3c, depicts the amount of time the QD spent in a
152 particular emission state. This QD exhibited no spectral dynamics, and the spectral-intensity
153 distribution contains only a single, well-defined feature. Such single-featured localization

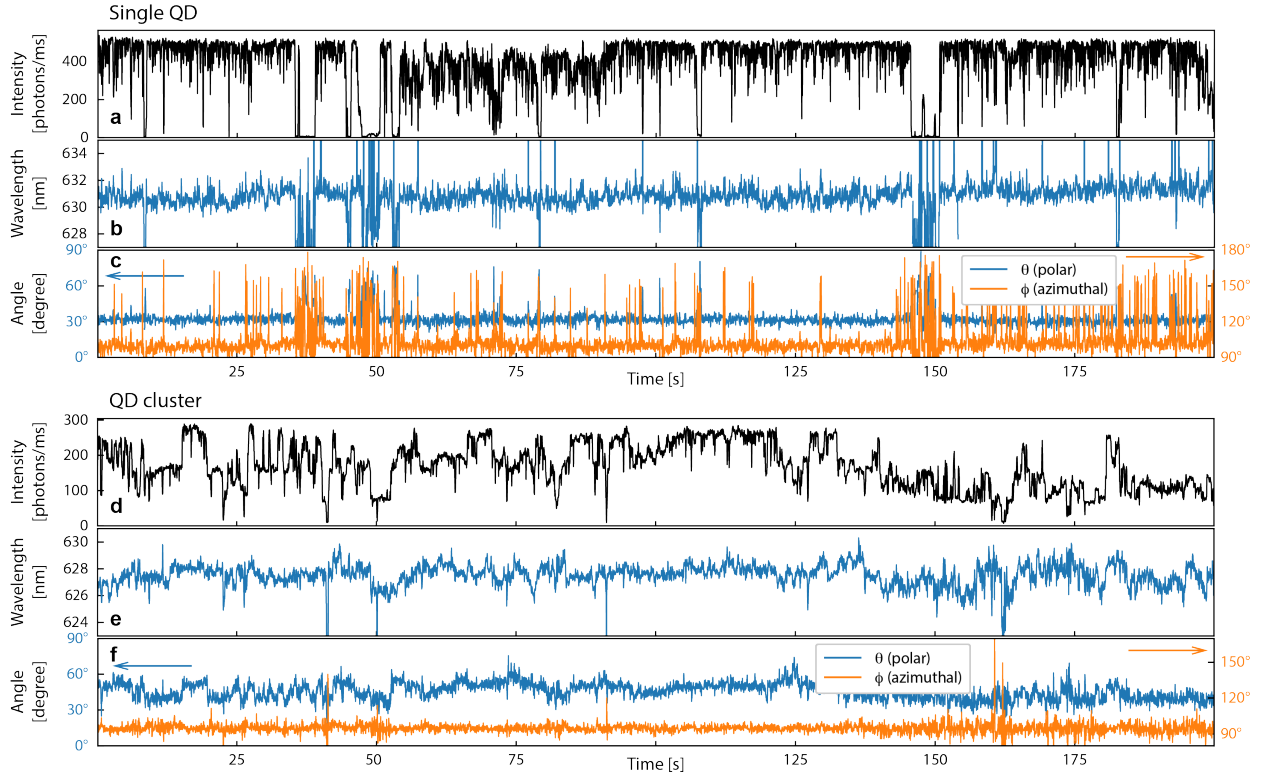


Figure 2: **Time traces of observed properties.** **a–c**, A representative single QD exhibits binary on/off intensity modulations (**a**). The emission wavelength (**b**) and the orientation of the 2D emission plane (**c**) for a single QD were constant throughout the measurement. **d–f**, A QD nanoassembly produces characteristically different intensity modulations (**d**) that are accompanied by discrete spectral changes (**e**), and changes to the polarization state of the emission (**f**).

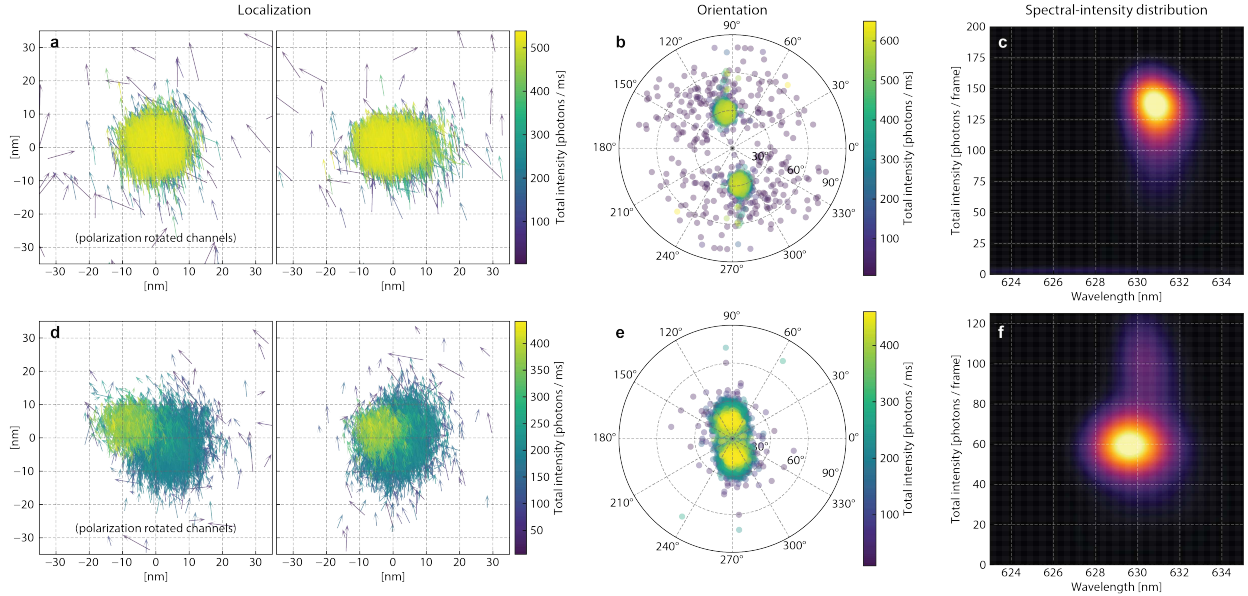


Figure 3: Super-resolution, orientation, and spectral signatures. **a–c**, A single QD has simple, single-featured localization (**a**), orientation (**b**), and spectral (**c**) signatures because these properties are linked to physical and unchanging properties of the QD. Left and right localization figures in (**a**) show the same QD, but are each based on corrected localizations from different polarization components. **d–f**, A small QD nanoassembly exhibits spatial variation to the emission intensity (**d**) with sub-regions of higher/lower intensity. While the emission polarization signature of the small nanoassembly (**e**) has a single feature, the spectral intensity distribution (**f**) shows higher emission intensities correlating with long wavelength emission and lower intensities correlating with short wavelength emission.

154 plots, orientation maps, and spectral-intensity distributions were observed among the other
 155 single QD analyzed in this study.

156 Figure 3d–f depicts another QD nanoassembly. Unlike a single QD, the spatial distribu-
 157 tion of the emission from this nanoassembly, Fig. 3d, is multi-featured, composed of regions
 158 with different intensity levels. The center-to-center difference of the two localization features
 159 is consistent with the 9.3 nm diameter of the QDs, suggesting this nanoassembly was a dimer.
 160 The spectral-intensity distribution, Fig. 3f, shows that a short amount of time was spent in
 161 a high intensity state at a longer wavelength than the more frequently visited lower intensity
 162 state. This correlation—high intensity with longer wavelength emission and lower intensity
 163 with shorter wavelength emission—is a signature of interactions due to FRET. An acceptor
 164 QD is the primary emitter, emitting at its intrinsic wavelength when all particles are active
 165 and funneling excitons to it, as well as when it is the only particle in an emitting state
 166 This creates multiple intensity levels at a longer wavelength. Shorter wavelength emission
 167 occurs when an acceptor QD is fluorescently dark and no longer overwhelming the emission
 168 that emanates from a donor particle before energy transfer occurs. Donor emission is lower

169 intensity because energy transfer diverts excitons to the acceptor particle. This FRET-only
170 interaction description is consistent with an interaction framework where a nanoassembly is
171 a composite object of individual emitters. The emission properties of individual particles
172 are distinct and maintain their identities, and the collective behavior of the group can be
173 described in terms of QDs as unaltered particles.

174 While the polarization signature in Fig. 3e implies an emission plane that has a small tilt
175 angle, and that the QDs in the cluster were aligned, such a polarization signature can also
176 be an indicator that the emission resembled an isotropic emitter because of a superposition
177 of multiple optical signals. As $\theta \rightarrow 0$, the intensity modulations among the polarization
178 components become small. Small or no intensity modulations is also a property of an isotropic
179 emitter. However, it is unlikely that this orientation signature was due to the super-position
180 of signals to resemble an isotropic emitter. The localization maps indicate two spatially
181 distinct features with different intensities but the same orientation. If this were a case of
182 the super-position of signals resembling an isotropic emitter, then the lower intensity levels
183 would contain fewer super-position components and the two localization features would have
184 different orientations as those components transitioned between bright and dark states, even
185 if the higher intensity feature projected a misleading isotropic signature.

186 Although the spatial distribution of the intensity and the spectral-intensity distribution
187 of the small nanoassembly are multi-featured, the orientation signature, Fig. 3e, shows a
188 single feature, indicating that one polarization state exists for the entire collection of QDs.
189 Similar singly- or narrowly-confined orientation signatures were found among nearly all of
190 the 33 QD nanoassemblies examined in detail. A single orientation feature is evidence
191 that either nanoassembly formation occurred with oriented attachment, or that neighboring
192 QDs influenced the polarization states of other QDs and generated a collective polarization
193 signature for the entire nanoassembly. The latter describes a decoupling of polarization
194 state with crystalline structure. An example of a non-interacting QD nanoassembly with
195 significantly different orientation and spectral features is given in Supplementary Fig. S15.

196 Large nanoassemblies, such as Fig. 4, offer a portrait of behavior that can occur locally
197 in larger structures such as films or aggregates. In this nanoassembly, emission is distributed
198 over 40 nm, a span that indicates this group contained a minimum of five QDs, but likely
199 more. This is a regime where many donor/acceptor relationships are possible, and any indi-
200 vidual QD in the group can have multiple neighbors that alter their local environment. The
201 spatial distribution of the intensity has multiple regions of different emission intensity, ex-
202 hibiting richer, more complicated features than the simpler small QD nanoassembly. Despite
203 the potential for multiple different orientation signatures, the orientation map, Fig. 4b, was a
204 single feature. Unlike the small nanoassembly that exhibited clear indications of FRET and
205 donor/acceptor relationships, the spectral-intensity distribution of this large nanoassembly,
206 Fig. 4c, was more ambiguous.

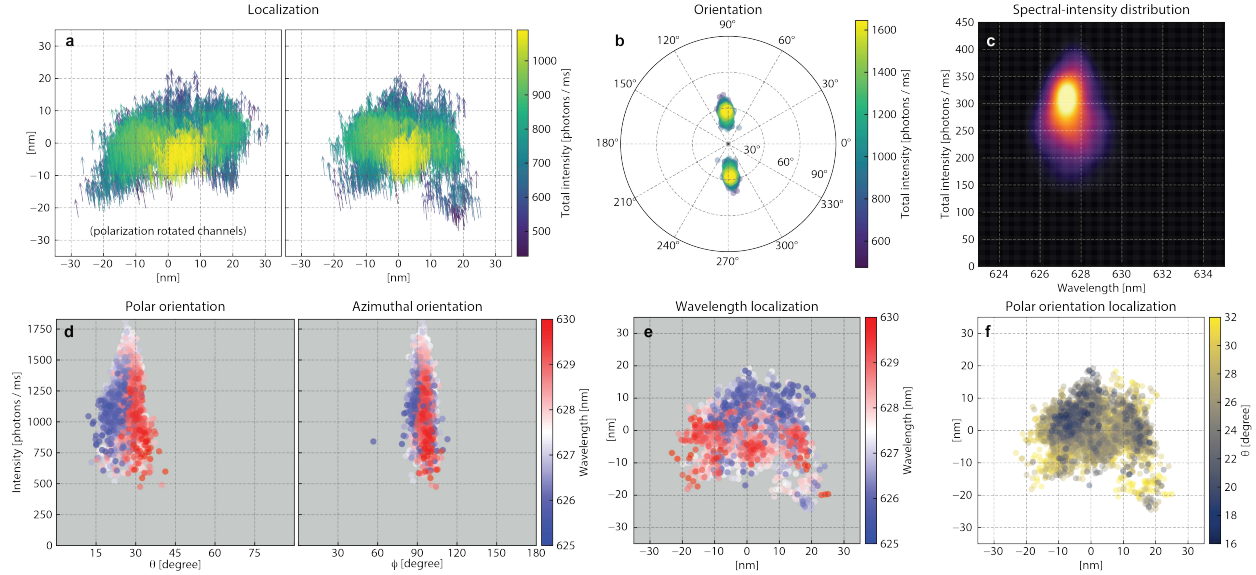


Figure 4: **Correlations from a large QD nanoassembly.** **a**, Super-resolution images of a large QD nanoassembly with intensity mapping suggest the physical layout of QDs in the nanoassembly, and show the spatial distributions of the various intensity levels. **b**, The emission plane orientation from the large QD nanoassembly is a single feature, despite the fluctuations of both position and intensity. **c**, For this large QD nanoassembly, the spectral-intensity distribution does not indicate a clear correlation. **d**, The small variation of the emission plane polar angle shows shorter wavelength emission (blue markers) comes from smaller polar tilt angles and longer wavelength emission (red markers) comes from more tilted emission planes. However, the emission wavelength and the azimuthal angle are uncorrelated (right figure). **e**, Mapping wavelength onto spatial positions shows the emission wavelength is correlated to specific sub-regions of the nanoassembly. **f**, Mapping the polar angle onto spatial positions does not indicate any correlation, and indicates the emission plane angle is uniform across the nanoassembly, despite other properties having spatial correlations.

207 Discussion

208 Although the spectral and polarization signatures of the large QD nanoassembly do not
209 depict detailed structure, correlations among these optical properties do. The narrow distri-
210 bution of θ was correlated with wavelength, Fig. 4d. Shorter wavelength emission corresponds
211 to a smaller tilt angle while the longer wavelength emission corresponds to a higher degree
212 of tilt. However, this correlation was not present in ϕ . Other QD nanoassemblies expressed
213 different orientation correlations (see Supplementary Fig. S16). Projections of the wave-
214 length onto the localizations, Fig. 4e, show that specific regions of the nanoassembly were
215 responsible for either the longer or shorter wavelength emission.

216 Significantly, the localization map of θ , Fig. 4f, was uniform over the entire nanoassembly.
217 This coherence was observed in all of the QD nanoassemblies examined, and extended as
218 far as 75 nm in the largest assembly. A common polarization signal from all regions of a
219 nanoassembly is an unexpected result, and implies the interactions between QDs coordinate
220 to generate this property. The permanent electrostatic dipole moments may produce this
221 phenomenon—either by oriented attachment (possibly unique to the clustering or deposition
222 steps), or by coupling to the emission dipole moments in a similar mechanism that QD
223 emission is manipulated by external fields. It is interesting that the c -axis orientations
224 implied by the polarization measurements do not correspond to the lowest energy alignment
225 of dipole moments: very few nanoassemblies had orientations along the optical axis ($\theta = 0$).

226 In conclusion, we developed a method to overcome bias introduced in wide-field polariza-
227 tion super-resolution microscopy, extended the approach to simultaneously capture spectral
228 information, and observed new collective behaviors from QD nanoassemblies. Although the
229 spectral properties were correlated with position within the nanoassemblies, orientation sig-
230 natures showed a single polarization state existed for an entire nanoassembly. Thus, QD
231 interactions produce a single coherent polarization signature. To our knowledge, this is the
232 first demonstration of mapping polarization and spectral signatures with nanometer preci-
233 sion.

234 Methods

235 QD synthesis and sample preparation

236 CdSe/CdS core/shell QDs were synthesized according to the methods described by[49]. This
237 method uses controlled, slow growth to produce high crystalline quality QDs with narrow size
238 dispersion. In our preparation, 4.6 nm diameter CdSe cores were capped with CdS, yielding
239 average QD diameters of 9.3 nm. QD emission was peaked at 636 nm. Stock solutions of QDs

240 were washed from the synthesis solution with several cycles of methanol precipitation and
241 resuspended in toluene for storage. Samples for fluorescence imaging were prepared by dilut-
242 ing the stock solution to nanomolar concentrations in toluene. For single QD measurements,
243 the nanomolar solution was directly spin-coated onto glass coverslips. QD nanoassemblies
244 were formed using previously reported methods[15, 17, 18]. Briefly, clusters were formed
245 by adding neat methanol (1% v/v) to the nanomolar QD solution for either one minute
246 (small clusters) or two minutes (large clusters) before spin coating the solution onto glass
247 coverslips. This process induces particle aggregation in solution, and the aggregates remain
248 attached during deposition. Previous correlated scanning electron microscopy (SEM) stud-
249 ies of this cluster preparation method showed the deposited aggregates contained 2–10 QDs,
250 arranged in 2D structures[18]. See Supplementary Section I for additional characterization
251 information.

252 **Imaging**

253 Samples were imaged on a modified Olympus IX-71 inverted microscope fitted with a 60×
254 UPlan Apo 1.5 NA objective (Olympus). We note that high-NA objectives can collect more
255 photons and improve localization precision, but are less sensitive for orientation imaging
256 because the large acceptance angles reduce the modulation depth of a signal. The internal
257 microscope tube lens was removed and the detection optical layout is shown in Fig. 1c.
258 To measure the polarization components at -45° and 45° , the fast axis of the half-wave
259 plate is oriented at 22.5° relative to the plane of the polarizing beamsplitter. The 250 mm
260 achromatic lenses (L2) produced images with effective magnifications of $70.6\times$. QDs were
261 excited by a 488 nm frequency-doubled continuous-wave diode laser (Coherent) in a total-
262 internal reflection configuration at 20 W/cm^2 . A custom autofocus, described in Han, *et*
263 *al.*[50], was used to maintain focus using a pick-off from the 488 nm excitation source. Image
264 sequences were captured at 50 ms exposure by two ProEM 512B EMCCD cameras (Princeton
265 Instruments) operating in external-triggering mode to synchronize frames. The cameras were
266 calibrated using a gain-series maximum-likelihood estimation (MLE) method to ensure the
267 relative intensities obtained from the two cameras were accurate[51].

268 **Localization analysis**

269 Diffraction-limited fluorescent spots that belonged to the same emitter were identified in each
270 polarization optical path and color channel. A single emitter produced eight spots per time
271 slice between the pair of camera images. Each spot was separately fit to an image model to
272 determine location and intensity. A custom MLE fitting algorithm that implements a robust
273 approximation of the EMCCD noise model (accurate at low and high signal levels) was used
274 to estimate parameters of the image model.

275 Because images produced by dipole emission depend on the orientation of the emitter and
 276 do not take a simple universal form, we employed a two-step residual approach to accurately
 277 determine the number of detected photons in a spot. A first pass fits all frames of an
 278 individual spot to a 2D pixel-integrated Gaussian PSF. A residual image was calculated from
 279 the difference of the estimated PSFs and image data in each frame, normalized, oversampled,
 280 centered, and averaged over the entire image sequence. The spots were then fit in a second
 281 pass to the sum of a 2D pixel-integrated Gaussian PSF with a fixed width and a spline-
 282 interpolation of the residual image. Thus, the combined PSF/residual accurately represents
 283 the number of photons in a spot. Each of the eight spots produced by a single emitter were fit
 284 with their own unique residual image. This approach also compensates for image aberrations
 285 in the final image model. A single residual image was valid for an entire sequence of images,
 286 and analyses from segments of image series verified the static behavior of the residuals.
 287 We found that orientation analysis using the first-pass fitting yielded essentially the same
 288 results as the residual-corrected fitting, likely because photon under-counting from using the
 289 2D pixel-integrated Gaussian is proportional to the true photon flux, so intensities extracted
 290 from each channel were proportionally biased. The residual images for several QDs and QD
 291 nanoassemblies are shown in Supplementary Fig. S14. Residuals differed across polarization
 292 channels, but were generally the same within a given polarization channel for all spots.

293 Position results were drift-corrected using the fiducial algorithm implemented in the
 294 software package ThunderSTORM[52]. Drifts were calculated from all spots in a given
 295 polarization/color channel, and each of the eight sub-images were corrected according to
 296 their own drift analysis.

297 Spectral analysis

298 Intensity values from the localization results were used to calculate spectral signatures. An
 299 emission wavelength per frame was calculated for each polarization channel, which were
 300 further composed of blue/red intensity pairs. Following the procedure outlined in[21], the
 301 peak emission wavelength was calculated from

$$\lambda_0(\eta) = a + b \times \text{erf}^{-1}(c \times \eta + d)$$

302 where the anisotropy value for a pair of color channels is given by

$$\eta = \frac{I_{i,\text{red}} - I_{i,\text{blue}}}{I_{i,\text{red}} + I_{i,\text{blue}}}.$$

303 $i = \{\text{S rot.}, \text{P rot.}, \text{S}, \text{P}\}$ indicates the polarization channel the color pair corresponds to,
 304 and the constants a , b , c , and d are determined by the spectral response curves of the
 305 optical system. The intensities $I_{i,j}$ here may refer to pixel intensities (for correction factor
 306 calculation) or the fit intensity values of a spot (for particle wavelength calculation), and
 307 are in units of photon number (*i.e.* scaled by camera gain values). From the QD synthesis

308 characterization reported in[49], the constants were determined using a single-particle QD
 309 spectral bandwidth of $\sigma = 10.2$ nm. Because the optical configuration depicted in Fig. 1c
 310 involves two transmissions/reflections through dichroic beamsplitters, the spectral response
 311 functions were replaced by $f_i(\lambda) \rightarrow f_i^2(\lambda)$ (*i.e.* $S_i(\lambda)$ of Eqn. (1) in[21]), where the spectral
 312 response functions are polarization-dependent and only include the dichroic beamsplitters
 313 as the LP filter is placed before all path separation optics. See Supplementary Section IV
 314 for additional details. The generation of the spectral-intensity distributions from intensity
 315 fit data is also outlined in[21].

316 Optical path calibration

317 Calculating orientation from the intensity distribution into different polarization components
 318 requires knowledge of the transmission efficiencies of each optical path to correct for uneven
 319 losses among the individual channels. For example, a 50/50 beamsplitter is never an exact
 320 50 % division into each path, and transmission through a half-wave plate or lens is never
 321 100 % due to absorption and reflection. Furthermore, such components have polarization-
 322 and wavelength-dependencies that can be difficult to measure once in their final installed
 323 alignments.

324 A sample that exhibits isotropic emission is necessary to determine the optical path
 325 efficiencies. Because transmission through each optical path is wavelength-dependent, the
 326 QDs used in this study were also used for calibration to match the spectral range and
 327 bandwidth. Ensemble measurements of a QD film were imaged to generate orientationally-
 328 averaged signals for each sub-image. Calibration images generated spatial correction maps
 329 over the entire fields of view for each image channel. We found similar calibration results
 330 from QD films and QDs imaged in solution, reinforcing the assumption that a film is a
 331 collection of randomly oriented particles. However, image bleeding among the sub-images
 332 due to imaging into the solution was evident, and the calibration results from QD films were
 333 used for analyses.

334 For isotropic emission, the intensity of each channel should be equal. Imposing this
 335 requirement, the spatially resolved correction factors are calculated according to

$$\delta_{i,j}(x, y, \lambda_i^{\text{film}}) = \frac{4I_{i,j}^{\text{film}}}{I_{\text{S rot.},j}^{\text{film}} + I_{\text{P rot.},j}^{\text{film}} + I_{\text{S},j}^{\text{film}} + I_{\text{P},j}^{\text{film}}}$$

336 where i again denotes the polarization channel and j refers to the color channel. Intensities
 337 are in units of photon number

$$I_{i,j}^{\text{film}}(x, y) = (I_{i,j}^{\text{film}} - I_{i,j}^{\text{dark}}) \times \frac{\text{ADU}_{i,j}}{\text{gain}_{i,j}}.$$

338 Subscripts on the ADU (analogue-to-digital conversion factor) and gain values reference the
 339 calibrations associated with the camera onto which the channel is imaged, and I^{dark} is the

340 dark image that specifies the camera offset values when not illuminated. The factor of 4
 341 and the terms in the denominator normalize the correction factors to all polarization chan-
 342 nels within a given color component. Alternatively, correction factors could be normalized
 343 within an orthogonal pair of polarization channels (*e.g.* only S and P channels), but in-
 344 cluding all polarization channels reduces noise in the correction factor maps. This approach
 345 accommodates several factors that can reduce the efficiency of an optical path, such as cam-
 346 era quantum efficiency or sensor dirt, as well as the transmission properties of the different
 347 optical components. See Supplementary Section V for an extended discussion about the
 348 correction factors.

349 Orientation analysis

350 The orientation of an emission spot is calculated from the intensity information of the local-
 351 ization fitting results, I^{QD} , using the Stokes parameters. Localization results from individual
 352 time slices combine to produce time-series trajectories of the azimuthal and polar angles, ϕ
 353 and θ . The Stokes parameters for orientation calculation are defined as

$$\begin{aligned}
 S_0 &= \sum_{i,j} I_{i,j}^{\text{QD}} \\
 S_1 &= \sum_j \frac{I_{\text{S rot.},j}^{\text{QD}}/\delta_{\text{S rot.},j} - I_{\text{P rot.},j}^{\text{QD}}/\delta_{\text{P rot.},j}}{S_0} \\
 S_2 &= \sum_j \frac{I_{\text{S},j}^{\text{QD}}/\delta_{\text{S},j} - I_{\text{P},j}^{\text{QD}}/\delta_{\text{P},j}}{S_0} \\
 p &= \sqrt{S_1^2 + S_2^2}
 \end{aligned}$$

354 where the summations over j incorporate the red and blue color channels into the same
 355 orientation calculation. The correction factors $\delta_{i,j}$ determined by calibration are valid at the
 356 wavelength of the QD film. However, the dichroics were selected to transition within the
 357 bandwidth of the QDs and their contribution to the optical path efficiencies are particularly
 358 sensitive to the wavelength of an individual QD emitter. Because the calibration QD film is
 359 spectrally red-shifted due to energy transfer, the correction factors $\delta_{i,j}$ must be evaluated at
 360 the wavelength of the QD

$$\delta_{i,j}(x, y, \lambda_i^{\text{QD}}) = \frac{f_i^2(\lambda^{\text{QD}})}{f_i^2(\lambda^{\text{film}})} \times \delta_{i,j}(x, y, \lambda_i^{\text{film}})$$

361 where f_i^2 is the instrument spectral response function used for the wavelength calculation.
 362 The ratio of the spectral response functions compensates for the loss differences due to
 363 the double-pass of the dichroic beamsplitters at the relevant wavelengths. The spectral re-
 364 sponses of the other optical elements in the detection path (50/50 beamsplitter, polarization

365 beamsplitter, and lenses) are relatively static in the spectral region where the QDs emit,
366 permitting this functional separation of the spectral response from the optical path effi-
367 ciencies calibration maps. Because the spectral signature of an emitter may change during a
368 measurement—particularly in QD nanoassemblies where emission from a QD with a different
369 spectral profile becomes dominant—the correction above is applied to data from individual
370 frames.

371 Using the Stokes parameters, the orientation angles are

$$\phi = \frac{1}{2} \tan^{-1} \left(\frac{S_1}{-S_2} \right)$$
$$\theta = P_{2D}^{-1}(p)$$

372 where P_{2D}^{-1} is the inverse of the modulation depth expression described by Lethiec, *et al.*[53]
373 for a 2D dipole emitter. For model parameters, we used an emitter ($\lambda = 630$ nm) on the
374 surface ($d = 0$ nm) of a glass substrate ($n = 1.518$), imaged through a 1.5 NA objective.
375 The negative sign in the denominator of the azimuthal angle ϕ aligns the value to the local
376 coordinate system of the microscope (relative to the x -axis) for a 2D dipole emitter. See
377 Supplementary Section III for additional details.

378 Acknowledgements

379 Research presented in this article was supported by the Laboratory Directed Research and
380 Development program of Los Alamos National Laboratory under project #20180189ER and
381 by the US Department of Energy (DOE) Biological and Environmental Research (BER)
382 Bioimaging Science Program (BSP). Additional support was provided by the Los Alamos Na-
383 tional Laboratory Institute for Materials Science Rapid Response Program. S. M. and J. A.
384 H. were funded by the US Department of Energy division of Energy Efficiency and Renewable
385 Energy (EERE), under grant #M615002955. This work was performed, in part, at the Cen-
386 ter for Integrated Nanotechnologies, an Office of Science User Facility operated for the U.S.
387 DOE Office of Science by Los Alamos National Laboratory (Contract 89233218CNA000001).
388 This research used resources provided by the Los Alamos National Laboratory Institutional
389 Computing Program. LA-UR-22-20078.

390 Author Contributions

391 A. v. O., P. G., and J. W. conceived the experiments, J. A. H. and S. M. synthesized the
392 quantum dot samples, M. G. provided technical guidance, D. R. and M. D. conducted the

393 experiments, and D. R. analyzed the results and prepared the manuscript. All authors
394 reviewed the manuscript.

395 Competing Interests

396 The authors declare no competing interests.

397 References

- 398 1. Cui, J. *et al.* Colloidal quantum dot molecules manifesting quantum coupling at room
399 temperature. *Nature Communications* **10**, 1–10 (2019).
- 400 2. Crisp, R. W., Schrauben, J. N., Beard, M. C., Luther, J. M. & Johnson, J. C. Coherent
401 Exciton Delocalization in Strongly Coupled Quantum Dot Arrays. *Nano Letters* **13**,
402 4862–4869 (2013).
- 403 3. Cohen, E. *et al.* Achieving Exciton Delocalization in Quantum Dot Aggregates Using
404 Organic Linker Molecules. *The Journal of Physical Chemistry Letters* **8**, 1014–1018
405 (2017).
- 406 4. Scholes, G. D. & Andrews, D. L. Resonance energy transfer and quantum dots. *Physical*
407 *Review B* **72**, 125331 (2005).
- 408 5. Nguyen, D., Nguyen, H. A., Lyding, J. W. & Gruebele, M. Imaging and Manipulat-
409 ing Energy Transfer Among Quantum Dots at Individual Dot Resolution. *ACS Nano*
410 (2017).
- 411 6. Chung, I., Shimizu, K. T. & Bawendi, M. G. Room temperature measurements of the
412 3D orientation of single CdSe quantum dots using polarization microscopy. *Proceedings*
413 *of the National Academy of Sciences* **100**, 405–408. pmid: 12515867 (2003).
- 414 7. Shim, M. & Guyot-Sionnest, P. Permanent dipole moment and charges in colloidal
415 semiconductor quantum dots. *The Journal of Chemical Physics* **111**, 6955–6964 (1999).
- 416 8. Nann, T. & Schneider, J. Origin of permanent electric dipole moments in wurtzite
417 nanocrystals. *Chemical Physics Letters* **384**, 150–152 (2004).
- 418 9. Park, S.-J., Link, S., Miller, W. L., Gesquiere, A. & Barbara, P. F. Effect of electric
419 field on the photoluminescence intensity of single CdSe nanocrystals. *Chemical Physics*
420 **341**, 169–174 (2007).
- 421 10. Galland, C. *et al.* Two types of luminescence blinking revealed by spectroelectrochem-
422 istry of single quantum dots. *Nature* **479**, 203–207 (2011).
- 423 11. Lorenz, S. *et al.* Orientation of Individual Anisotropic Nanocrystals Identified by Po-
424 larization Fingerprint. *ACS Nano* (2021).

- 425 12. Klokkenburg, M. *et al.* Dipolar Structures in Colloidal Dispersions of PbSe and CdSe
426 Quantum Dots. *Nano Letters* **7**, 2931–2936 (2007).
- 427 13. Vanmaekelbergh, D. Self-assembly of colloidal nanocrystals as route to novel classes of
428 nanostructured materials. *Nano Today* **6**, 419–437 (2011).
- 429 14. Yu, M. & Van Orden, A. Enhanced Fluorescence Intermittency of CdSe-ZnS Quantum-
430 Dot Clusters. *Physical Review Letters* **97**, 237402 (2006).
- 431 15. Shepherd, D. P. *et al.* Fluorescence Intermittency and Energy Transfer in Small Clusters
432 of Semiconductor Quantum Dots. *The Journal of Physical Chemistry C* **114**, 14831–
433 14837 (2010).
- 434 16. Baer, R. & Rabani, E. Theory of resonance energy transfer involving nanocrystals: The
435 role of high multipoles. *The Journal of Chemical Physics* **128**, 184710 (2008).
- 436 17. Whitcomb, K. J., Geisenhoff, J. Q., Ryan, D. P., Gelfand, M. P. & Van Orden, A.
437 Photon Antibunching in Small Clusters of CdSe/ZnS Core/Shell Quantum Dots. *The*
438 *Journal of Physical Chemistry B* **119**, 9020–9028 (2015).
- 439 18. Ryan, D. P. *et al.* Mapping Emission from Clusters of CdSe/ZnS Nanoparticles. *The*
440 *Journal of Physical Chemistry C* **122**, 4046–4053 (2018).
- 441 19. Dunlap, M. K. *et al.* Super-resolution photoluminescence lifetime and intensity mapping
442 of interacting CdSe/CdS quantum dots. *Applied Physics Letters* **116**, 021103 (2020).
- 443 20. Xu, X. *et al.* Assembly and Separation of Semiconductor Quantum Dot Dimers and
444 Trimers. *Journal of the American Chemical Society* **133**, 18062–18065 (2011).
- 445 21. Ryan, D. P. *et al.* A framework for quantitative analysis of spectral data in two channels.
446 *Applied Physics Letters* **117**, 024101 (2020).
- 447 22. Lv, B. *et al.* Photon antibunching in a cluster of giant CdSe/CdS nanocrystals. *Nature*
448 *Communications* **9**, 1536 (2018).
- 449 23. Backlund, M. P., Lew, M. D., Backer, A. S., Sahl, S. J. & Moerner, W. E. The Role of
450 Molecular Dipole Orientation in Single-Molecule Fluorescence Microscopy and Impli-
451 cations for Super-Resolution Imaging. *ChemPhysChem* **15**, 587–599 (2014).
- 452 24. Zhanghao, K., Gao, J., Jin, D., Zhang, X. & Xi, P. Super-resolution fluorescence polar-
453 ization microscopy. *Journal of Innovative Optical Health Sciences* **11**, 1730002 (2017).
- 454 25. Aguet, F., Geissbühler, S., Märki, I., Lasser, T. & Unser, M. Super-resolution orienta-
455 tion estimation and localization of fluorescent dipoles using 3-D steerable filters. *Optics*
456 *Express* **17**, 6829 (2009).
- 457 26. Backer, A. S., Backlund, M. P., von Diezmann, A. R., Sahl, S. J. & Moerner, W. E. A
458 bisected pupil for studying single-molecule orientational dynamics and its application
459 to three-dimensional super-resolution microscopy. *Applied Physics Letters* **104**, 193701
460 (2014).
- 461 27. Backer, A. S. & Moerner, W. E. Extending Single-Molecule Microscopy Using Optical
462 Fourier Processing. *The Journal of Physical Chemistry B* **118**, 8313–8329 (2014).

- 463 28. Backer, A. S. & Moerner, W. E. Determining the rotational mobility of a single molecule
464 from a single image: a numerical study. *Optics Express* **23**, 4255–4276 (2015).
- 465 29. Mazidi, H., King, E. S., Zhang, O., Nehorai, A. & Lew, M. D. *Dense Super-Resolution*
466 *Imaging of Molecular Orientation Via Joint Sparse Basis Deconvolution and Spatial*
467 *Pooling* in *2019 IEEE 16th International Symposium on Biomedical Imaging (ISBI*
468 *2019)* 2019 IEEE 16th International Symposium on Biomedical Imaging (ISBI 2019)
469 (2019), 325–329.
- 470 30. Zhanghao, K. *et al.* Super-resolution imaging of fluorescent dipoles via polarized struc-
471 tured illumination microscopy. *Nature Communications* **10**. pmid: 31619676 (2019).
- 472 31. Curcio, V., Alemán-Castañeda, L. A., Brown, T. G., Brasselet, S. & Alonso, M. A.
473 Birefringent Fourier filtering for single molecule coordinate and height super-resolution
474 imaging with dithering and orientation. *Nature Communications* **11**, 5307 (2020).
- 475 32. Ding, T. *et al.* Single-molecule orientation localization microscopy for resolving struc-
476 tural heterogeneities between amyloid fibrils. *Optica* **7**, 602–607 (2020).
- 477 33. Rimoli, C. V., Cruz, C. A. V., Curcio, V., Mavrikakis, M. & Brasselet, S. 4polar-STORM
478 polarized super-resolution imaging of actin filament organization in cells. *bioRxiv*, 2021.03.17.435879
479 (2021).
- 480 34. Böhmer, M. & Enderlein, J. Orientation imaging of single molecules by wide-field epifluo-
481 rescence microscopy. *Journal of the Optical Society of America B* **20**, 554–559 (2003).
- 482 35. Patra, D., Gregor, I. & Enderlein, J. Image Analysis of Defocused Single-Molecule
483 Images for Three-Dimensional Molecule Orientation Studies. *The Journal of Physical*
484 *Chemistry A* **108**, 6836–6841 (2004).
- 485 36. Cyphersmith, A. *et al.* Disentangling the role of linear transition dipole in band-edge
486 emission from single CdSe/ZnS quantum dots: Combined linear anisotropy and defo-
487 cused emission pattern imaging. *Applied Physics Letters* **97**, 121915 (2010).
- 488 37. Katoh, T. A. *et al.* Angle change of the A-domain in a single SERCA1a molecule
489 detected by defocused orientation imaging. *Scientific Reports* **11**, 13672 (1 2021).
- 490 38. Cruz, C. A. V. *et al.* Quantitative nanoscale imaging of orientational order in biological
491 filaments by polarized superresolution microscopy. *Proceedings of the National Academy*
492 *of Sciences* **113**, E820–E828. pmid: 26831082 (2016).
- 493 39. DeMay, B. S. *et al.* Septin filaments exhibit a dynamic, paired organization that is
494 conserved from yeast to mammals. *Journal of Cell Biology* **193**, 1065–1081 (2011).
- 495 40. Ohmachi, M. *et al.* Fluorescence microscopy for simultaneous observation of 3D orien-
496 tation and movement and its application to quantum rod-tagged myosin V. *Proceedings*
497 *of the National Academy of Sciences* **109**, 5294–5298. pmid: 22431610 (2012).
- 498 41. Mehta, S. B. *et al.* Dissection of molecular assembly dynamics by tracking orientation
499 and position of single molecules in live cells. *Proceedings of the National Academy of*
500 *Sciences* **113**, E6352–E6361. pmid: 27679846 (2016).

- 501 42. Zhang, Z., Kenny, S. J., Hauser, M., Li, W. & Xu, K. Ultrahigh-throughput single-
502 molecule spectroscopy and spectrally resolved super-resolution microscopy. *Nature Meth-*
503 *ods* **12**, 935–938 (2015).
- 504 43. Dong, B., Song, K.-H., Davis, J. L., Zhang, H. F. & Sun, C. Sub-10 nm Distance Mea-
505 surements between Fluorophores using Photon-Accumulation Enhanced Reconstruc-
506 tion. *Advanced Photonics Research* **1**, 2000038 (2020).
- 507 44. Webb, S. E. D. *et al.* Simultaneous widefield single molecule orientation and FRET
508 microscopy in cells. *Optics Express* **16**, 20258–20265 (2008).
- 509 45. Montiel, D. & Yang, H. Observation of Correlated Emission Intensity and Polarization
510 Fluctuations in Single CdSe/ZnS Quantum Dots†. *The Journal of Physical Chemistry*
511 *A* **112**, 9352–9355 (2008).
- 512 46. Htoon, H., Furis, M., Crooker, S. A., Jeong, S. & Klimov, V. I. Linearly polarized ‘fine
513 structure’ of the bright exciton state in individual CdSe nanocrystal quantum dots.
514 *Physical Review B* **77**, 035328 (2008).
- 515 47. Chizhik, A. I., Chizhik, A. M., Khoptyar, D., Baer, S. & Meixner, A. J. Excitation
516 Isotropy of Single CdSe/ZnS Nanocrystals. *Nano Letters* **11**, 1131–1135 (2011).
- 517 48. Spinicelli, P. *et al.* Bright and Grey States in CdSe-CdS Nanocrystals Exhibiting Strongly
518 Reduced Blinking. *Physical Review Letters* **102**, 136801 (2009).
- 519 49. Chen, O. *et al.* Compact high-quality CdSe–CdS core–shell nanocrystals with narrow
520 emission linewidths and suppressed blinking. *Nature Materials* **12**, 445 (2013).
- 521 50. Han, J. J., Kunde, Y. A., Hong-Geller, E. & Werner, J. H. Actin restructuring dur-
522 ing Salmonella typhimurium infection investigated by confocal and super-resolution
523 microscopy. *Journal of Biomedical Optics* **19**, 016011–016011 (2014).
- 524 51. Ryan, D. P. *et al.* A gain series method for accurate EMCCD calibration. *Scientific*
525 *Reports* **11**, 18348 (1 2021).
- 526 52. Ovesný, M., Křížek, P., Borkovec, J., Svindrych, Z. & Hagen, G. M. ThunderSTORM:
527 a comprehensive ImageJ plug-in for PALM and STORM data analysis and super-
528 resolution imaging. *Bioinformatics (Oxford, England)* **30**, 2389–2390. pmid: 24771516
529 (2014).
- 530 53. Lethiec, C. *et al.* Measurement of Three-Dimensional Dipole Orientation of a Single Flu-
531 orescent Nanoemitter by Emission Polarization Analysis. *Physical Review X* **4**, 021037
532 (2014).

Supplementary Files

This is a list of supplementary files associated with this preprint. Click to download.

- [naturecommsQDpolarizationS1rev2.pdf](#)